

Motion simulation of radio-labeled cells in whole-body positron emission tomography

Nils Marquardt, Tobias Hengsbach, Marco Mauritz, Benedikt Wirth, and Klaus Schäfers

Abstract—Cell tracking is a subject of active research gathering great interest in medicine and biology. Positron emission tomography (PET) is well suited for tracking radio-labeled cells in vivo due to its exceptional sensitivity and whole-body capability. For validation, ground-truth data is desirable that realistically mimics the flow of cells in a clinical situation. This study develops a workflow (CeFloPS) for simulating moving radio-labeled cells in a human phantom. From the XCAT phantom, the blood vessels are reduced to nodal networks along which cells can move and distribute to organs and tissues. The movement is directed by the blood flow which is calculated in each node using the Hagen-Poiseuille equation and Kirchhoff's laws assuming laminar flow. Organs are voxelized and movement of cells from artery entry to vein exit is generated via a biased 3D random walk. The probabilities of whether cells move or stay in tissues are derived from rate constants of physiologically based compartment modeling. PET listmode data is generated using the Monte-Carlo simulation framework GATE based on the definition of a large-body PET scanner with cell paths as moving radioactive sources and the XCAT phantom providing attenuation data. From the flow simulation of 10000 cells, 100 sample cells were further processed by GATE and listmode data was reconstructed into images for comparison. As demonstrated by comparisons of simulated and reconstructed cell distributions, CeFloPS can realistically simulate the cell behavior of whole-body PET providing valuable data for development and validation of cell tracking algorithms.

I. INTRODUCTION

CELL IMAGING and tracking is a subject of active research gathering great interest in the medical and biomedical science community. Non-invasive imaging techniques using fluorescent or luminescent markers in optical imaging (OI), iron oxide particles in magnetic resonance imaging (MRI), or radio-labelled tracers in single photon emission computed tomography (SPECT) and positron emission tomography (PET) have been frequently used in preclinical

This work has been submitted to the IEEE for possible publication. Copyright may be transferred without notice, after which this version may no longer be accessible.

This work was funded by the Deutsche Forschungsgemeinschaft (DFG) – CRC 1450 – 431460824.

N. Marquardt, T. Hengsbach and K. Schäfers are with the European Institute for Molecular Imaging, University of Münster, 48149 Münster, Germany (e-mail: n.marquardt@uni-muenster.de; thengsba@uni-muenster.de; schafkl@uni-muenster.de).

M. Mauritz and B. Wirth are with the Institute for Computational and Applied Mathematics, University of Münster, 48149 Münster, Germany (e-mail: marco.mauritz@uni-muenster.de; benedikt.wirth@uni-muenster.de).

studies to permit in vivo visualization of living cells [1]. For human application, MRI, PET and SPECT are the most promising tools as they provide either high spatial resolution (MRI) or excellent whole-body sensitivity (PET, SPECT). Of these imaging modalities, PET has become of special interest following labelled immune cells in the context of stem cell imaging and cell-based therapies [2].

PET is particularly advantageous because it combines exceptional sensitivity with the possibility of whole-body coverage which has been further advanced in recent years by the design of large-body PET systems with extended coverage of the axial field-of-view in the range of 1 to 2 meters, improved time-of-flight capabilities and excellent system sensitivities [3]. Using either long-lived isotopes or reporter genes, immunoPET has great potential to identify biomarkers allowing to treat patients based on their most likely response to a dedicated immunotherapy [4]–[6].

Following the idea of PET-based particle tracking developed originally for technical applications, the outstanding sensitivity of PET was recently used to track radio-labeled singular cells [7]–[10]. In this context, a new image reconstruction algorithm for PET was introduced by our group using an optimal transport based regularization technique [11] showing great potential for tracking single and multiple radio-labeled cells within a human body scenario.

The current study is concerned with the development of a software workflow to accurately simulate the movement of radio-labeled cells within the human body in a clinical setting. This workflow generates dynamic cell flow data, which is then used in Monte Carlo simulations to model the underlying PET physics. Since the location and motion of the cells are known at all times, the cell flow PET simulation (CeFloPS) serves as ground-truth data for the development and validation of novel image reconstruction and tracking tools.

II. METHODS

A. Simulation basis

CeFloPS is based on a special version of the XCAT phantom with high resolution 3D models of all organs, blood vessels, bones and muscles (Fig. 1a) in the form of STEP files [12, 13]. Using Inventor (Version 2023, Autodesk Inc., San Rafael, USA), these STEP files were converted into StL files (StereoLithography file format), providing triangulated surface meshes of all organs and structures. The StL files were further processed in Python (Version 3.11.5, Python

Software Foundation) with the help of the trimesh library [14], allowing for operations on the meshes and giving access to the coordinates of the vertices. For further processing, meshes of all muscles and internal organs were converted into voxelized volumes with voxel size $0.5 \text{ mm} \times 0.5 \text{ mm} \times 0.5 \text{ mm}$, while the complex anatomy of blood vessel meshes was simplified by reducing it to node networks. The nodes describe the possible paths a cell can take and are placed along the central axis of a blood vessel, storing information about (i) its spatial coordinates, (ii) which nodes are adjacent in the direction of blood flow and (iii) the radius of the blood vessel.

To generate the nodes, the blood vessels were divided into segments starting from one end point of a vessel. For each segment, the barycenter was formed of all vertices located in this segment, resulting in points lying inside a blood vessel. Starting from the first point inside a blood vessel, planes, orthogonal to the blood vessel, were then placed at an interval of 1 mm along the vectors between these points. Using the intersection of those planes with the blood vessel surface, the vessel radius and the new center point were calculated, resulting in the final 1 mm spaced nodes positions (see Fig. 2).

Nodes that lie at bifurcations of blood vessels and thus have more than one neighbor in the direction of blood flow were marked and are in the following referred to as links. Since the spatial resolution of the XCAT phantom is limited, some connections between vessels are missing, as seen in Fig. 1b. In this case we interpolate linearly between the nodes of those vessels to generate a connection. In addition, the spatial resolution of blood vessels varies from organ to organ. The smallest radius defined in XCAT is 0.15 mm and is located in the toes. Consequently, no capillary bed is included that connects the nodes of arteries and veins. (Fig. 1c). This results in a total of five separate networks of nodes: arteries, veins, portal vein, and pulmonary arteries and veins, all of which, except for the portal vein, are connected via the heart. In order to compensate for the lack of capillaries, these separate networks are artificially combined to form a single closed network in which opposing arteries and veins leading to the same organ are virtually connected.

B. Blood flow simulation

From the node networks, the mean blood flow rate \bar{Q}_i as well as the vessel resistance R_i were estimated for each node i from a highly simplified flow model using Kirchhoff's laws in combination with the Hagen-Poiseuille equation. This was done by assuming laminar flow in every vessel, treated as a cylinder [15, 16]:

$$\bar{Q}_i = \frac{\Delta P_i}{R_i}, \quad (1)$$

$$R_i = \frac{8\eta l_i}{\pi r_i^4}, \quad (2)$$

$$R_{\text{tot}} = \sum_{i=1}^n R_i \quad (3)$$

for serial connections of vessels and

$$\frac{1}{R_{\text{tot}}} = \sum_{i=1}^n \frac{1}{R_i} \quad (4)$$

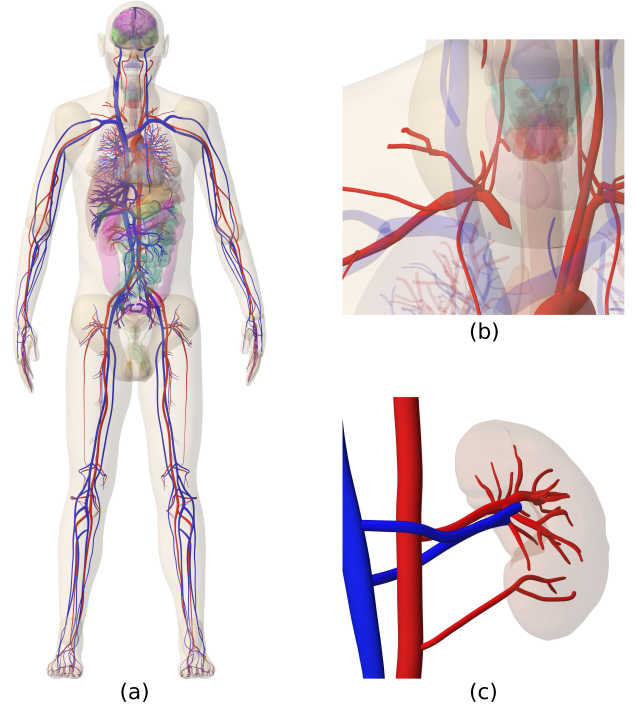


Fig. 1. Mesh representation of the XCAT phantom defining vessel structures and organs (a). Only the larger vessels are defined by XCAT showing partly missing connections (b) and a just coarsely defined capillary bed (c).

for parallel connections, with ΔP_i the blood pressure difference, l_i the distance between two nodes, r_i the radius of the vessel at the node position, n the number of nodes in a branch and η the dynamic viscosity of blood. The calculations were performed under the assumption of a cardiac output of 100 ml/s, a mean arterial blood pressure of 100 mmHg in the part of the aorta in close proximity to the heart, and 0 mmHg in the vena cava entering the heart. Furthermore, a constant blood viscosity of 3.5 mPa·s was presumed. Due to the lack of small blood vessels in the XCAT phantom, our flow model misses a large portion of high resistances which would add to the calculation of the total resistance R_{tot} in (3) and (4). By (1), this also affects the blood flow \bar{Q}_i in each node. To compensate for this, we arbitrarily scaled the radii we determined in each node by a factor of 0.7 as this was found to lead to more realistic values for \bar{Q}_i .

At a link, the probability p_{node} with which a cell will move to the next possible node is calculated based on the blood flow \bar{Q}_{link} in the link and $\bar{Q}_{\text{node},i}$ in each following node:

$$p_{\text{node},i} = \frac{\bar{Q}_{\text{node},i}}{\bar{Q}_{\text{link}}} \quad \text{with} \quad \bar{Q}_{\text{link}} = \sum_{i=1}^n \bar{Q}_{\text{node},i} \quad (5)$$

and n the number of following nodes of a link.

The individual velocity of a single cell is assigned by pseudo-random number sampling based on a cumulative distribution function (CDF). This ensures that a group of cells starting from the same node have different velocities and disperse over time in the blood vessels. The CDF was derived

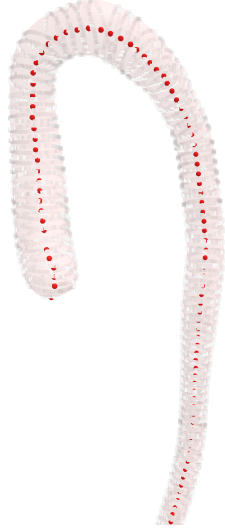


Fig. 2. XCAT based mesh of the aorta together with the node representation (red dots) calculated from orthogonal planes. Each node stores information about next node neighbors, blood flow direction, and vessel radius.

using the velocity profile of laminar flow in a tube [17]

$$v(x) = v_{\max} \left(1 - \frac{x^2}{r^2}\right) \quad \text{with} \quad v_{\max} = \frac{r^2 \Delta P}{4\eta l} = \frac{2\bar{Q}}{\pi r^2}, \quad (6)$$

where $x \in [0, r]$ is the radial distance from the center. The distribution of blood flow over the profile of the vessels is then given by

$$\frac{dQ(x)}{dx} = 2\pi x v(x). \quad (7)$$

Division by the mean blood flow rate yields the probability density function (PDF)

$$f_p(x) = \frac{1}{Q} \frac{dQ}{dx} = \frac{4x}{r^2} \left(1 - \frac{x^2}{r^2}\right) \quad \text{with} \quad \int_0^r f_p(x) dx = 1, \quad (8)$$

which by integration leads to the CDF:

$$F_p(x) = \int_0^x f_p(t) dt = \frac{x^2}{r^2} \left(2 - \frac{x^2}{r^2}\right). \quad (9)$$

The velocity of a cell is then obtained by (6) with a randomly picked x according to (9).

C. Organ distribution simulation

Inside a voxelized organ, cell motion is guided by a biased 3D random walk along the voxels to simulate the capillary bed and the tissue exchange. This process is carried out in a series of discrete calculations, each with a defined time step. The current simulations have set the time step to 600 ms. To commence, voxels containing an artery entrance or a vein exit were identified and subsequently referred to as start-voxels and end-voxels, respectively. If an organ does not have an artery entrance and/or vein exit due to missing connections in the XCAT phantom, the nearest artery/vein is calculated and the closest voxel to that blood vessel is determined as start-/end-voxel.

Remaining blood vessels are connected to an organ in the same way if their distance to that organ lies within a 2 cm threshold. To compensate for missing arterial branches in muscles and organs, each node of the arteries and veins can serve as entrance and exit for cells, respectively. For every voxel within an organ or muscle, direction vectors towards all start- and end-voxels were determined along with separate weighting values. As the distance d between a voxel and its start/end voxel increases, these weightings decrease by a factor of $1/d^2$, as shown in Fig. 3. The direction of the vectors is pointing away from start-voxel or towards end-voxel. The combination of those vectors represents the most probable directions for a cell to move. The weightings of vectors in start- and end-voxels were set to zero.

The random walk is initiated at a start-voxel, where a cell can move to one of the surrounding voxels. This gives 26 possible directions (provided the start-voxel does not reside on the organ's periphery), all with the same probability. For the proceeding steps, the direction is biased in accordance with the previously determined weightings of the direction vectors in each voxel. If a cell reaches an end-voxel, the random walk concludes, followed by the cell exiting via the vein back into the nodal network for further blood flow simulation.

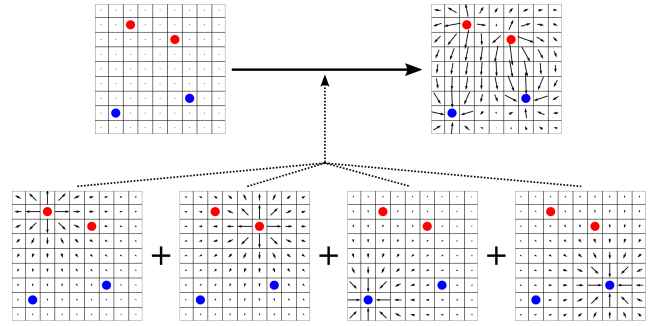


Fig. 3. Principle of a biased random walk for a single cell defined by arterial sources (red) and venous sinks (blue) (top left). For each voxel, the most probable direction vector (top right) is calculated by superimposing attracting and repellent vectors for each start- and end-point (bottom).

Besides the biased random walk, a compartment model was implemented in the organ distribution simulation which governs the duration a cell stays in an organ. In each organ voxel a cell can be located in different virtual compartments. The exchange between compartments is determined by rate constants k_i which also define the probabilities of whether a cell moves during the next time step or not. The number and structure of these compartments as well as the values of the rate constants are depending on the pharmacokinetics and physiology of the cell and the organ. This information must be known in advance to the CeFloPS simulation.

As a first example and as proof-of-principle, we implemented a two-compartment ^{18}F -Fluorodesoxyglucose (FDG) model as shown in Fig. 4. The simulated cells in this example therefore do not behave like real, existing cells, but like an FDG tracer. For this two-compartment model, C_1 and C_2 denote the unbound and bound states of an FDG molecule

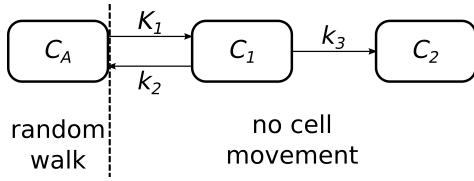


Fig. 4. The movement of cells within each organ is regulated by compartmental models, which determine the probability of a cell undergoing a random walk or being constrained to a virtual compartment.

in tissue and C_A the free FDG molecule in the blood supply of the tissue. As long as cells are located in C_A they undergo the random walk. If they enter C_1 or C_2 , they stay at their position and do not move. The change in amount of cells in these compartments in dependency on the (arterial) blood C_A can be described by the differential equations

$$\left[\begin{aligned} \frac{d}{dt} C_A(t) &= -K_1 C_A(t) + k_2 C_1(t), \\ \frac{d}{dt} C_1(t) &= K_1 C_A(t) - (k_2 + k_3) C_1(t) \quad \text{and} \\ \frac{d}{dt} C_2(t) &= k_3 C_1(t). \end{aligned} \right] \quad (10)$$

The differential equation for C_A is put into brackets as usually C_A is a measured quantity and not a compartment like C_1 and C_2 . For a better understanding of how the movement probabilities of a cell are derived, we still list the equations for C_A as a compartment. In this example, the values of the rate constants K_1 , k_2 , and k_3 are taken from [18] and listed in Table I.

TABLE I
VALUES OF RATE CONSTANTS TAKEN FROM [18] USED IN THE SIMULATION

Tissue	K_1 [ml/min/ml]	k_2 [min^{-1}]	k_3 [min^{-1}]
lung	0.023	0.205	0.001
liver	0.660	0.765	0.002
spleen	1.593	2.867	0.006
gray matter	0.107	0.165	0.067
myocardium	0.832	2.651	0.099
muscle	0.026	0.249	0.016
rest ^a	0.553	1.213	0.039

^a For organs not included in [18] the rate constants were set to the values of "all regions".

The differential equations in (10) can be analytically solved, yielding the following solutions for C_A and C_1 :

$$\left[\begin{aligned} C_A(t) &= k_2 C_1(t) * e^{-K_1 t}, \\ C_1(t) &= K_1 C_A(t) * e^{-(k_2 + k_3)t}, \end{aligned} \right] \quad (11)$$

where $*$ denotes the convolution operator. Since the solutions in (11) are linear combinations of exponential functions, we describe the time-dependent probability of transitions between compartments by the following equations based on the CDFs

of exponential distributions:

$$\begin{aligned} p_{C_A \rightarrow C_1}(t) &= 1 - e^{-K_1 t}, \\ p_{C_1 \rightarrow C_A}(t) &= \frac{k_2}{k_2 + k_3} \left(1 - e^{-(k_2 + k_3)t} \right) \quad \text{and} \\ p_{C_1 \rightarrow C_2}(t) &= \frac{k_3}{k_2 + k_3} \left(1 - e^{-(k_2 + k_3)t} \right). \end{aligned} \quad (12)$$

The equations in (12) indicate the probability of a transition between two compartments occurring from the beginning of the simulation up to time t . Based on these equations, a random decision is made at each time step as to whether a cell transitions or not. Cells entering a tissue are first located in the blood compartment C_A . As long as cells are in C_A they undergo the (biased) random walk in the organ. Cells that have transitioned into C_1 do not partake in the random walk but stay at their position. For these cells, the decision is made after each step as to whether they go back to C_A and are able to move again or whether they stay in C_1 or transition to C_2 . A cell that transitions from C_1 back to C_A is considered to be in the venous blood and undergoes random walk until reaching an end-voxel, without the possibility to reenter C_1 . If cells enter C_2 , they remain trapped in their position for the rest of the simulation and do no longer move.

For the FDG simulation, the paths and distributions of 10000 cells are simulated in parallel. For every time step, the organ and compartment in which each cell is located is recorded. This allows the generation of time profiles of cells in tissues. For a given tissue, the tissue concentration of cells per milliliter or the corresponding cell number (as the sum in C_1 and C_2) is calculated. The number of cells in the blood is made up of all cells that are still in the node network or in a C_A compartment of an organ.

D. PET simulation

Raw PET data is generated using the Geant4 application for tomographic emission GATE (version 9.0) [19, 20]. The cell paths outputs from the CeFloPS simulations have the format of GATE placement files and thus are used as generic moving sources in the simulations. The sources, i.e. the cells, are simulated as spheres whose diameters and activities can be specified by the user. For the example shown in this work, a diameter of 10 μm and an activity of 1 kBq per cell were simulated for 100 cells. This activity per cell and number of cells does not correspond to a realistic scenario and was only chosen to serve as a proof-of-principle. The PET scanner used in the simulation is based on the Siemens Biograph Vision Quadra (Siemens Healthineers, Erlangen, Germany), a large-body PET system using approximately 250000 single lutetium oxyorthosilicate (LSO) detector elements covering an axial field of view (FOV) of 106 cm [21]. The background radiation in the scanner generated by the presence of ^{176}Lu in the LSO crystals can be simulated if desired but was neglected in the current simulation. The attenuation map for gamma energies of 511 keV provided by the XCAT phantom was used as an attenuation phantom. The attenuation phantom was placed in the PET scanner so that the upper body including the head were in the FOV of the scanner. Since the simulated cell

paths are based on the blood vessel and organ structure of the XCAT phantom, their positions correspond exactly to the anatomical structures in the attenuation phantom, making the simulation also realistic in view of the proportion of attenuated and scattered events. Although the lower body exceeds the FOV of the scanner, it is still simulated in case a cell is located there.

III. RESULTS

Starting at the aorta with a mean blood flow of 100 ml/s, the blood distributes into all vessels and tissues depending on the resistances of the vessel system and the blood pressure differences (as listed exemplarily in Table II). It is evident that the lungs receive all blood through the contraction of the right myocardium, which accounts for 100 % of the total blood flow. The main venous vessels, in contrast, share their blood flow, which is then fed into the right myocardium (inferior vena cava - 89 %, superior vena cava - 11 %). Notably, the kidneys receive a disproportionately higher blood flow than expected (46 %), with the left kidney's blood flow (33 %) being more than twice as high as the right one (13%). This behavior is due to insufficient definition of the vascular structure of the kidneys and is further discussed later.

The biased 3D random walk that cells perform when they migrate from the blood into a tissue is illustrated in Fig. 5 using the example of the lung. Starting from arterial end-points (sources, red dots), cells follow random pathways (green dots) until they exit into a vein end-point (input, blue dots), or stay in a defined compartment. The biased random walk ensures that the entire organ tissue is potentially accessible by incoming cells.

TABLE II

BLOOD FLOW DISTRIBUTION CALCULATED BY CEFLOPS

Blood vessel or organ	Percentage of total blood flow ^a
aorta	100 %
inferior vena cava	89 %
superior vena cava	11 %
lung	100 %
left	47 %
right	53 %
kidneys	46 %
left	33 %
right	13 %
liver	11 %
spleen	0.7 %
pancreas	0.7 %

^aFor a cardiac output of 100 ml/s.

Fig. 6 illustrates the locations of 100 simulated cells within a node system at six time points, compared to maximum intensity projections (MIPs) reconstructed from PET data using an expectation maximization (EM) algorithm without attenuation correction. The reconstructed positions and cell counts align well with ground-truth positions, despite minor reconstruction artifacts in the MIPs causing low-intensity signals outside the body due to missing attenuation and scatter correction. Initially, cells (red spheres) are injected into the left arm vein (median cubital) over three seconds. After six seconds, cells migrate towards the left clavicle, appearing as a single dark spot in the MIP, making individual cells indistinguishable. By

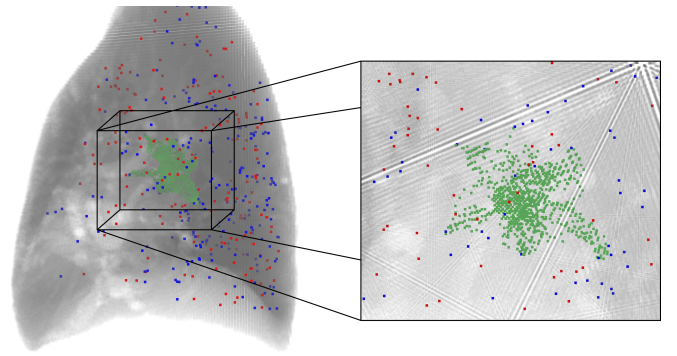


Fig. 5. Examples for a biased 3D random walk of 100 cells in the lung. Starting from voxels with arterial sources (red) in the middle of the right picture, the cells travel to various venous sinks (blue), with the voxels along the way marked in green.

18 seconds, most cells distribute within the lung, with some transitioning to arterial blood, allowing individual cells and clusters to be distinguishable in the MIP. After 30 seconds, cells predominantly remain in the lung; some transition to compartments C_1 or C_2 , changing color from red to green, while others disperse through the abdominal cavity and neck, identifiable in the MIP. At one minute, cells migrate further into the torso, with some returning to venous blood and lungs, and individual cells reach the head, right arm, and left leg (outside the scanner's FOV). After five minutes, cells disperse body-wide, with some transitioning to compartment C_1 and C_2 , as seen in cells in the right arm; one cell remains, while the other leaves the arm. This dispersion continues over ten minutes, increasing the proportion of stationary cells in compartment C_1 and C_2 , thus facilitating the identification of individual cells in MIPs over time due to wider distribution and fewer clusters.

Figs. 7 and 8 illustrate the temporal distribution of cells in arterial blood, lung, kidneys, liver, spleen, and a lesion as absolute cell numbers and as cell concentrations per milliliter, respectively. The lesion in this case is the pancreas, for which the value of k_3 was set to 2.071 min^{-1} in order to simulate increased trapping of cells in a tissue. In the initial 15 seconds of the simulation, the organs and arterial blood show no signal, as the cells were still within the venous blood. Following this interval, the arrival of the cell bolus in the arterial blood, lungs, kidneys, and liver can be identified as peaks. These peaks subsequently decline when cells that have not transitioned from C_A to compartment C_1 leave the organs after a brief period. No peak can be identified in the lesion, where the cell count and concentration rises steadily after the first entry of cells. In the case of the spleen, a peak can only be observed in terms of concentration, as the absolute number of cells is quite low (below 5). In the arterial blood, two initial peaks can be observed occurring shortly before and after the peak of lung entry. The initial peak is relatively brief and may be attributed to the passage of cells through the pulmonary arteries. The second peak can be identified as the point at which the cell bolus enters the arterial blood from the left ventricle. At approximately 80, 115, and 150 seconds, further peaks are visible in the arterial blood before the cell count and

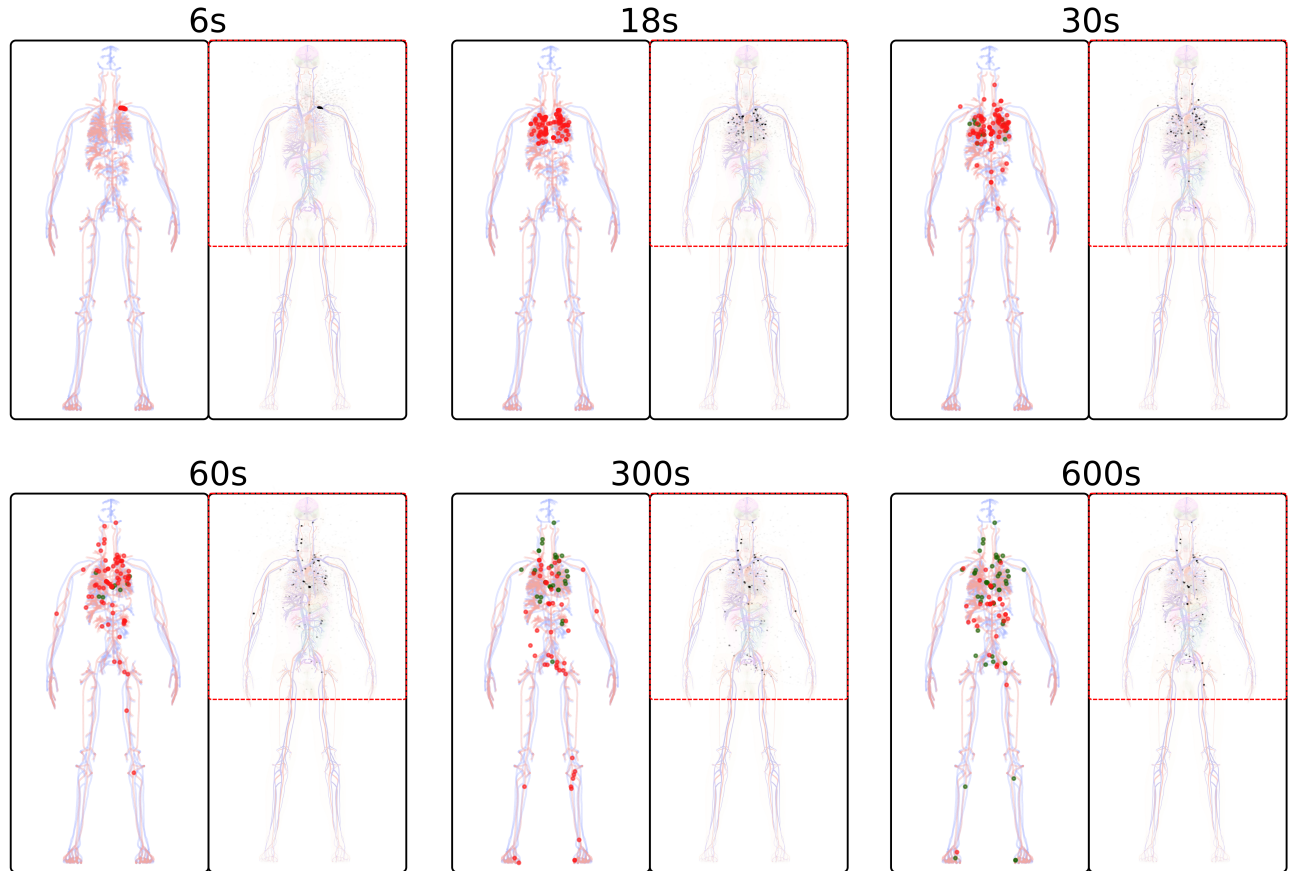


Fig. 6. Comparison of simulated ground-truth cell positions and reconstructed PET data for 100 cells at six different time points showing the positions of both moving cells (red, left) in the node system as well as stationary cells that have entered C_1 or C_2 (green, left). The reconstructed PET maximum intensity projections (right) show the cell distribution (black) superimposed to the organ and blood vessel structure. The red dotted line marks the FOV of the simulated PET scanner.

concentration decrease continuously. These peaks represent the cycle of the cell bolus through the entire blood system once more, before distributing homogeneously in the blood.

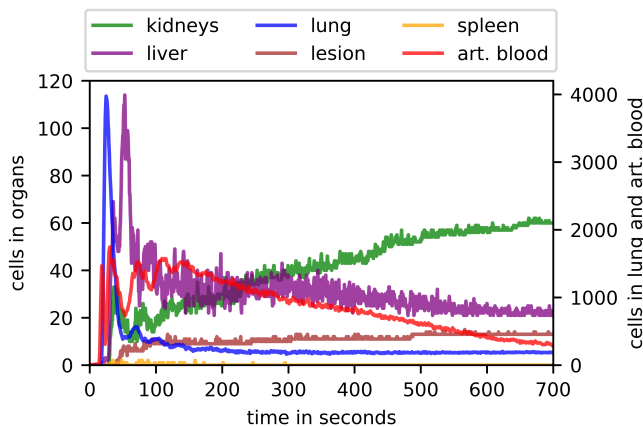


Fig. 7. Simulated number of cells over time in arterial blood and selected tissues. Note the different scale for lung and arterial blood.

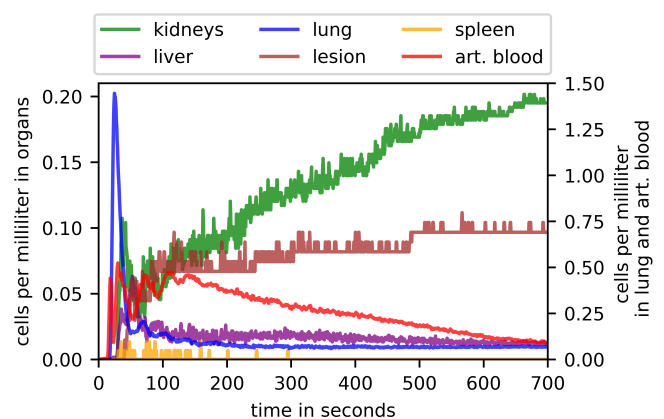


Fig. 8. Simulated cell concentrations (cells per milliliter) over time for arterial blood and specific tissues. Note the different scale for lung and arterial blood.

IV. DISCUSSION

The here presented simulation framework, CeFloPS, has been demonstrated to be capable of simulating realistic cell

pathways within the human body, which can be utilized for the development of image reconstruction algorithms as well as specific cell tracking strategies. CeFloPS allows to simulate not only the realistic flow of cells through the vessel branches but also the migration of cells from the vasculature into tissues either as reversible or non-reversible trapping steps. By that, different physiologically relevant scenarios can be simulated for various cell types providing realistic data for mimicking the dynamic distribution of cells within the human body. Beyond pure cell-based simulations, even tracer studies could be simulated by CeFloPS, as shown here by the FDG example. Following the CeFloPS simulations, a label can be assigned to the cells, which was chosen for PET studies as a radio-label (β^+ emitter) but could be of any kind allowing also simulations for other imaging modalities, such as SPECT, OI, MRI, or ultrasound imaging.

The simulation of PET physics was performed by GATE using a large-body PET system where radioactivity was attributed to each individual cell, defined as a small ball. Since this post-processing step is independent of the CeFloPS simulation, any other simulation framework could also be used which is capable of processing dynamic source distributions. In this study, only one bed position of 106 cm length defined by a large-body PET was simulated leading to an incomplete coverage of the entire human body. However, this could easily be extended towards a multi-bed simulation or using a total-body PET system covering a larger FOV.

The radioactivity of 1 kBq attributed to each FDG “cell” in the example is quite high and not realistic in the context of cell tracking experiments. In any case, this served only as a proof-of-principle value allowing a relatively noise-free dynamic image reconstruction of the simulated PET data for comparison with ground-truth cell positions. For realistic cell tracking simulation, radioactivity values in the range of a few Bq would be more appropriate. However, the demonstration of cell trajectory based PET reconstructions for low-count data, as shown before by our group (see [11]), was not part of this work and will be subject of subsequent studies.

It is evident from the cell numbers (Fig. 7 and Fig. 8) that certain organs are preferentially traversed by cells over others. This is due to the fact that the probability of which blood vessel branch is chosen at bifurcations is dependent upon the proportion of blood flow, as illustrated by (5). Organs that are less likely to be traversed by cells will therefore have a lower cell count. Conversely, this explains why the lungs and arterial blood, through which all cells pass, have such a high number of cells and concentration. As stated above, the kidneys receive a disproportionately high blood flow (see Table II), which is reflected in the organ’s highest cell concentration at the end of the simulation as seen in Fig. 8. This is due to the rudimentary modeling of the blood vessels in the kidneys by XCAT, exhibiting a lack of small diameter vessels (see Fig. 1c). Given that these represent a significant resistance, as indicated by (2), the blood flow to the kidneys is currently overestimated. Consequently, the likelihood of cell paths traversing the kidneys is greater than that of other organs. The spatial resolution of the XCAT phantom thus represents a clear limitation of CeFloPS. In order to improve towards

a more realistic behavior, two potential approaches could be followed. Either, missing smaller blood vessels could be added to the XCAT phantom which would lead to a higher resistance in the vasculature and thus to a more realistic blood flow. Or, pre-defined resistances could be attributed to dedicated organs which would also lead to a more realistic flow simulation in CeFloPS. In principle, a different anthropomorphic phantom with higher level of details could also be implemented in the CeFloPS framework which could circumvent the flow imbalances.

Blood flow is currently implemented as a continuous mean flow, completely ignoring the pulsating characteristics of the blood circulation. This is no limitation for the purpose of our study, but could be of interest when focusing on local effects due to the pulse wave behavior. Also, turbulent flow and a variable blood viscosity which is known to play an important role in the area of the capillary bed, are completely ignored. Moreover, cells in our study are considered as small particles which freely flow through the blood system and freely diffuse through the tissue compartments. Cell specific behaviors, such as rolling or adhesion at the endothelium or immune related activation cannot explicitly be modeled within the CeFloPS simulation. However, a similar behavior of cells could potentially be modeled by setting (dynamic) k -Parameters (Tab. I) for compartmental exchanges.

V. CONCLUSION

In this study, we presented the development of a cell flow PET simulation (CeFloPS) that is capable of accurately simulating the behavior of injected radio-labeled cells during human whole-body PET imaging with ground-truth knowledge of the cells’ positions. The data obtained with CeFloPS is of significant value for the development and validation of cell tracking algorithms, with the potential to contribute to a deeper understanding of immune system-related processes or to the guidance of cell-based therapies.

VI. ACKNOWLEDGMENT

We greatly acknowledge the help of Paul Segars for providing an extended version of XCAT with precise vessel and tissue definitions.

REFERENCES

- [1] M. F. Kircher, S. S. Gambhir, and J. Grimm, “Noninvasive cell-tracking methods.” *Nature reviews. Clinical oncology*, vol. 8, pp. 677–88, 9 2011.
- [2] V. Ponomarev, “Advancing immune and cell-based therapies through imaging,” *Molecular Imaging and Biology*, vol. 19, pp. 379–384, 2017.
- [3] S. R. Cherry, T. Jones, J. S. Karp, J. Qi, W. W. Moses, and R. D. Badawi, “Total-body PET: Maximizing sensitivity to create new opportunities for clinical research and patient care,” *Journal of Nuclear Medicine*, vol. 59, pp. 3–12, 1 2018.
- [4] I. Friberger *et al.*, “Comparative in vivo biodistribution of cells labelled with [89Zr]Zr-(oxinate)4 or [89Zr]Zr-dfo-ncs using PET,” *EJNMMI Research*, vol. 13, p. 73, 8 2023.
- [5] K. O. Jung *et al.*, “Whole-body tracking of single cells via positron emission tomography,” *Nature Biomedical Engineering*, vol. 4, pp. 835–844, 6 2020.
- [6] L. Melendez-Alafort, G. Ferro-Flores, L. D. Nardo, B. Ocampo-García, and C. Bolzati, “Zirconium immune-complexes for PET molecular imaging: Current status and prospects,” *Coordination Chemistry Reviews*, vol. 479, p. 215005, 3 2023.

- [7] D. Hampel, S. Manger, D. Parker, and T. K. Wheldon, "Superpept: A new tool for positron emission particle tracking; first results," *Nuclear Instruments and Methods in Physics Research Section A: Accelerators, Spectrometers, Detectors and Associated Equipment*, vol. 1028, p. 166254, 4 2022.
- [8] Y. Ouyang, T. J. Kim, and G. Pratz, "Evaluation of a BGO-based PET system for single-cell tracking performance by simulation and phantom studies," *Molecular Imaging*, vol. 15, p. 153601211664648, 1 2016.
- [9] S. Ghosh and P. Das, "Single-cell tracking with Compton-PET: An in silico feasibility study," *Nuclear Instruments and Methods in Physics Research Section A: Accelerators, Spectrometers, Detectors and Associated Equipment*, vol. 1053, p. 168373, 8 2023.
- [10] H. T. M. Nguyen *et al.*, "Ultrasensitive and multiplexed tracking of single cells using whole-body PET/CT," *Science Advances*, vol. 10, 6 2024.
- [11] B. Schmitzer, K. P. Schäfers, and B. Wirth, "Dynamic cell imaging in PET with optimal transport regularization," *IEEE Transactions on Medical Imaging*, vol. 39, no. 5, pp. 1626–1635, 2019.
- [12] W. P. Segars, G. Sturgeon, S. Mendonca, J. Grimes, and B. M. Tsui, "4d xcat phantom for multimodality imaging research," *Medical physics*, vol. 37, no. 9, pp. 4902–4915, 2010.
- [13] International Organization for Standardization, *Industrial automation systems and integration — Product data representation and exchange: Part 21: Implementation methods: Clear text encoding of the exchange structure*, ISO 10303-21:2016(E) ed. Vernier, Geneva, Switzerland: International Organization for Standardization, 2016. [Online]. Available: <https://www.iso.org/standard/63141.html>
- [14] M. Dawson-Haggerty *et al.*, "trimesh 4.4.1." [Online]. Available: <https://trimesh.org/>
- [15] R. Lampe, N. Botkin, V. Turova, T. Blumenstein, and A. Alves-Pinto, "Mathematical modelling of cerebral blood circulation and cerebral autoregulation: Towards preventing intracranial hemorrhages in preterm newborns," *Computational and Mathematical Methods in Medicine*, vol. 2014, no. 1, p. 965275, 2014.
- [16] J. H. Helthuis *et al.*, "A patient-specific cerebral blood flow model," *Journal of Biomechanics*, vol. 98, p. 109445, 2020.
- [17] A. Belhocine, "Numerical study of heat transfer in fully developed laminar flow inside a circular tube," *The International Journal of Advanced Manufacturing Technology*, vol. 85, pp. 2681–2692, 2016.
- [18] E. J. Li *et al.*, "Efficient delay correction for total-body PET kinetic modeling using pulse timing methods," *Journal of Nuclear Medicine*, vol. 63, no. 8, pp. 1266–1273, 2022.
- [19] S. Agostinelli *et al.*, "GEANT4—a simulation toolkit," *Nuclear instruments and methods in physics research section A: Accelerators, Spectrometers, Detectors and Associated Equipment*, vol. 506, no. 3, pp. 250–303, 2003.
- [20] S. Jan *et al.*, "GATE: a simulation toolkit for PET and SPECT," *Physics in Medicine & Biology*, vol. 49, no. 19, p. 4543, 2004.
- [21] G. A. Prenosil *et al.*, "Performance characteristics of the biograph vision quadra PET/CT system with a long axial field of view using the NEMA NU 2-2018 standard," *Journal of nuclear medicine*, vol. 63, no. 3, pp. 476–484, 2022.